Nanoscale
Advances

PAPER

View Article Online
View Journal | View Issue

Cite this: *Nanoscale Adv.*, 2023, 5, 6194

Tuning the morphology, stability and optical properties of $CsSnBr_3$ nanocrystals through bismuth doping for visible-light-driven applications†

Md. Asif Adib, Fahmida Sharmin and M. A. Basith*

Received 8th May 2023
Accepted 30th September 2023

DOI: 10.1039/d3na00309d

rsc.li/nanoscale-advances

In this investigation, we have demonstrated the synthesis of lead-free $CsSnBr_3$ (CSB) and 5 mol% bismuth (Bi) doped CSB (CSB′B) nanocrystals, with a stable cubic perovskite structure following a facile hot injection technique. The Bi substitution in CSB was found to play a vital role in reducing the size of the nanocrystals significantly, from 316 ± 93 to 87 ± 22 nm. Additionally, Bi doping has inhibited the oxidation of Sn^{2+} of CSB perovskite. A reduction in the optical band gap from 1.89 to 1.73 eV was observed for CSB′B and the PL intensity was quenched due to the introduction of the Bi^{3+} dopant. To demonstrate one of the visible-light-driven applications of the nanocrystals, photodegradation experiments were carried out as a test case. Interestingly, under UV-vis irradiation, the degradation efficiency of CSB′B was roughly one order lower than that of P25 titania nanoparticles; however, it was almost five times higher when driven by visible light under identical conditions. The water stability of CSB′B perovskite and suppression of the oxidative degradation of Sn were confirmed through XRD and XPS analyses after photocatalysis. Moreover, by employing experimental parameters, DFT-based first-principles calculations were performed, which demonstrated an excellent qualitative agreement between experimental and theoretical outcomes. The as-synthesized Bi-doped CSB might be a stable halide perovskite with potential in visible-light-driven applications.

1 Introduction

Metal halide perovskites (MHPs), with the chemical formula ABX_3 (where A and B are cations and X is a halogen anion), are currently the subject of extensive research owing to their attractive optoelectronic properties such as high absorption coefficients, direct band gap, long carrier lifetime, high carrier mobility, *etc.*[1,2] However, state-of-the-art perovskites such as $CH_3NH_3PbI_3$, $HC(NH_2)PbI_3$, *etc.*, are limited in large-scale commercialization due to the instability of organic A-site cations and the probability of leaching carcinogenic Pb into the environment.[3,4] As a result, significant effort is being made to develop total inorganic, lead-free MHPs with enhanced chemical stability. In this regard, several cations such as Sn(II), Ge(II), Ag(I), Sb(III), and Ti(IV) are being widely investigated as the potential replacement of Pb(II) ions.[5–7] Among these candidates, Sn(II) has attracted sincere attention since it shares the same group in the periodic table and hence the same valence electronic configuration (ns^2 np^2) as Pb.[8] Thus, total inorganic, Sn-based perovskites such as $CsSnX_3$ exhibit similar or even somewhat better optoelectronic properties compared to their lead-based counterparts.[9] Particularly, Sn-based perovskite $CsSnBr_3$ has attracted attention owing to its better stability, higher charge mobilities, and narrow band gap.[10,11]

Notably, several investigations revealed that, under direct exposure to moisture, Sn in tin-based halide perovskites rapidly transforms to Sn^{4+} from Sn^{2+} resulting in a thermally stable but optoelectronically inactive state.[12,13] Therefore, the stability of $CsSnBr_3$ requires further improvements. Among several attempts to improve the stability of MHPs, substitutional doping at the B-site with divalent or trivalent elements like Mg^{2+}, Pd^{2+}, Sb^{3+}, Eu^{3+}, Bi^{3+}, *etc.*, has been reported as an established strategy to fabricate stable Sn-based MHPs.[9,14,15] Particularly, Bi doping at the B site of Sn-based MHPs has reportedly demonstrated its ability to inhibit the phase transition, tune the optical band gap, increase the charge carrier density, and thus enhance its optoelectronic performance.[16–18]

The synthesis of $CsSnBr_3$ with the desired phase is quite challenging due to the strong moisture affinity of the core Sn ions.[12,19] A previous investigation[20] reported the time and cost-efficient synthesis of $CsSnBr_3$ *via* a mechanochemical route; however, the agglomerated particles revealed their limitations. In another investigation,[21] $CsSnBr_3$ was synthesized following a chemical process, but it required a very long drying time to obtain a powder sample. Among several techniques for the

---

Nanotechnology Research Laboratory, Department of Physics, Bangladesh University of Engineering and Technology, Dhaka-1000, Bangladesh. E-mail: mabasith@phy.buet.ac.bd

† Electronic supplementary information (ESI) available. See DOI: https://doi.org/10.1039/d3na00309d

successful fabrication of $CsSnBr_3$ or similar perovskites, the hot injection technique has been mentioned as a time-efficient chemical approach in a number of previous investigations.[22,23] This method has been reported to yield required materials with improved morphology and stability, and especially the synthesized samples were highly pure with good crystallinity.[24,25]

In this present investigation, to improve the stability and optical properties of $CsSnBr_3$ (CSB), a nominal amount of Bi (5 mol%) was doped at the B-site. The doping percentage was set at 5 mol% considering several earlier investigations, which demonstrated the formation of secondary phases at higher doping percentages.[18,26] Both undoped and Bi-doped CSB nanocrystals were synthesized following a facile hot injection technique to extensively investigate their physico-chemical properties. Notably, MHPs are being widely implemented in various applications such as solar cells, light emitting diodes, photodetectors, *etc.*, because of their fascinating optoelectronic properties.[27] These characteristics also make MHPs suitable candidates for photocatalytic applications involving the conversion of solar energy into chemical energy.[28] As a result, the photocatalytic performance of these materials was widely investigated. However, the most extensively studied MHPs for photocatalytic applications such as organic dye degradation and hydrogen production were mostly Pb-based.[29–31] To the best of our knowledge, the photocatalytic performance of lead-free Bi-doped $CsSnBr_3$ (CSB′B) prepared following the hot injection technique is yet to be investigated. Therefore, in this study, we have synthesized both CSB and CSB′B samples following the hot injection technique with a promising morphology to investigate and compare their physico-chemical properties, and finally to assess their potential application in water remediation. We have investigated the photocatalytic performances of the lead-free CSB and CSB′B samples following the degradation of an organic dye. Additionally, we elucidated the dye degradation mechanism by the CSB′B sample and its ability to degrade the colorless pollutant ciprofloxacin to examine whether the degradation is truly photocatalytic or due to a dye-sensitizing effect. Moreover, the stability of such Sn-based MHP systems in an aqueous medium is a major challenge; therefore, we conducted XRD and XPS analyses on the collected catalyst after the completion of the photocatalytic experiment to check the water stability.

Notably, at the molecular level, it is quite challenging to experimentally observe the effect of doping on various properties of nanocrystals. Therefore, by using experimentally obtained parameters, we have performed Density Functional Theory (DFT) calculations to provide some insights into the effect of bismuth doping on the physical and photocatalytic properties of the CSB sample.[17,24]

2 Experimental and computational details

2.1 Experimental

2.1.1 Materials. Cs_2CO_3 (Sigma-Aldrich, 99.9%), $SnBr_2$ (Sigma-Aldrich), $BiBr_3$ (Sigma-Aldrich, ≥98%), oleic acid (OA, Sigma-Aldrich, 90%), oleylamine (OAm, Sigma-Aldrich, 70%), 1-octadecene (ODE, Sigma-Aldrich, 90%), *n*-hexane (PT Smart Lab, research grade), ethyl acetate (EtOAc, PT Smart Lab, research grade), polyvinylidene fluoride (PVDF, Sigma-Aldrich), 1-methyl-2-pyrrolidone (NMP, Sigma-Aldrich), and Na_2SO_4 (Sigma-Aldrich) were used as received without further purification unless otherwise noted.

2.1.2 Synthesis method. The synthesis of $CsSn_{1-x}Bi_xBr_3$ (where $x = 0.00$, 5.0, 10.0 mol%) was conducted using a facile hot injection technique.[22]

2.1.3 Synthesis of Cs-oleate as the cesium precursor. Cs_2CO_3 (0.407 g), OA (1.3 ml), and ODE (20 ml) were loaded into a 250 ml 3-neck flask and stirred under vacuum for 1 h at 120 °C. Afterward, the flask was purged with Ar gas for 5 min and placed under a vacuum. This process of alternatively applying a vacuum and an Ar flow was repeated a total of three times to remove moisture and O_2. The reaction was considered complete when the solution appeared clear, indicating that all the Cs_2CO_3 had reacted with the OA.[32] The Cs-oleate solution in ODE was stored in Ar until it was required for the next synthesis step.

2.1.4 Synthesis of colloidal $CsSn_{1-x}Bi_xBr_3$. In this stage, a stoichiometric amount of $SnBr_2$, $BiBr_3$, and 50 ml of ODE was taken in a 250 ml flask (conc. 38 mmol) and degassed under a vacuum at 120 °C for 1 h. After that, the flask was placed under a constant Ar gas flow, and 5 ml of OA and OAm were injected. The flask was kept under vacuum again until the solutes ($SnBr_2$ and $BiBr_3$) dissolved completely, and the solution did not release any gas. The Ar gas flow was restarted, and the temperature was set to rise to 160 °C. At this stage, Cs-oleate (8 ml) pre-heated to 70 °C was swiftly injected into the reaction mixture. After a fixed time (cut-off time), the reaction was quenched by the immediate immersion of the flask into an ice-cooled water bath.

2.1.5 Isolation of the prepared samples. The solvent–antisolvent precipitation method[33] was implemented for the separation of the prepared materials and EtOAc was chosen as a suitable antisolvent for the isolation method. At first, the as-prepared colloidal solution containing $CsSn_{1-x}Bi_xBr_3$ was mixed with EtOAc at a ratio of 1 : 3 and centrifuged at 8000 rpm for 5 min. Next, the nanocrystals were redispersed in a solution containing *n*-hexane and EtOAc at a ratio of 1 : 2 and centrifuged for 5 min. Afterward, the supernatant was discarded and the precipitation was disseminated in 20 ml of EtOAc and centrifuged again at 8000 rpm for 5 min. The supernatant was discarded and the precipitation was again dispersed in 5 ml of *n*-hexane and centrifuged at 8500 rpm for 5 min. Finally, the supernatant was collected as the purified products. Fig. 1 shows the schematic synthesis steps for the preparation of CSB nanocrystals.

2.2 Characterization

The crystal structure of the as-prepared samples was investigated by obtaining their powder XRD patterns using a diffractometer (Rigaku SmartLab) with a Cu X-ray source (wavelength, $\lambda = K\alpha_1 = 1.5405$ Å and $K\alpha_2 = 1.5418$ Å). Furthermore, the crystallographic parameters and phases of the synthesized

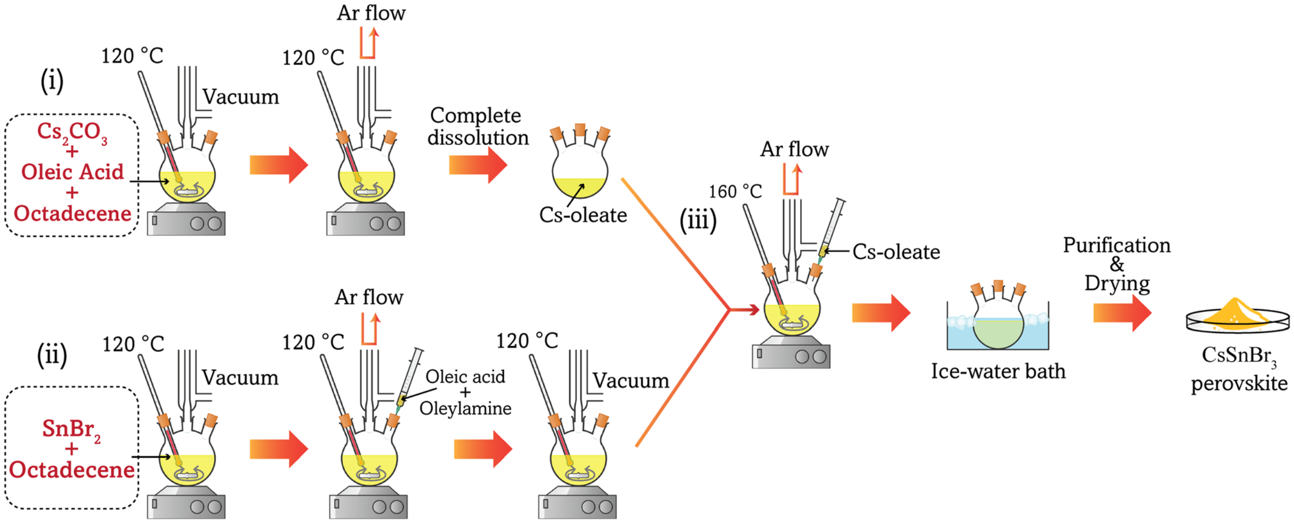

Fig. 1 Schematic representation of the synthesis steps of CSB nanocrystals using the hot injection technique.

perovskites were analyzed by Rietveld refinement of the XRD pattern using FullProf software.[34] The thermal stability of the prepared samples was characterized by thermogravimetric analysis (TGA) under an N_2 atmosphere at a heating rate of 10 °C min^{-1}. The surface morphology and elemental composition of the CSB and CSB′B samples were investigated using field emission scanning electron microscopy (FESEM) (JEOL, JSM-7600F, Japan). Further investigation on the morphology was carried out using transmission electron microscopy (TEM) (Talos F200X, Thermo Fisher Scientific, USA). Additionally, the SAED pattern was analyzed using the CrysTBox software suite.[35] The chemical states and binding energy of the individual elements were characterized by X-ray photoelectron spectroscopy (XPS) (Thermo Fisher Scientific, USA). Moreover, an ultraviolet-visible (UV-vis) spectrophotometer (UV-2600, Shimadzu, Japan) was used to obtain the reflectance and absorbance spectra of the prepared samples. The steady-state photoluminescence (PL) spectra of the samples were obtained using a photoluminescence spectrofluorophotometer (RF 6000, Shimadzu, Japan) with an excitation wavelength of 400 nm at room temperature. The photocatalytic dye degradation efficiency of CSB and CSB′B was evaluated *via* the degradation of rhodamine B (RhB), and ciprofloxacin (CIP) under solar irradiation. The details of the photocatalytic experiments are provided in the ESI (S1–S3†). Mott–Schottky measurements and electrochemical impedance spectroscopy (EIS) of CSB and CSB′B samples were performed at room temperature *via* an electrochemical workstation (Autolab PGSTAT302N, Metrohm, Germany) using a standard three-electrode system. The details of electrochemical measurements are addressed in ESI S4.†

2.3 Water stability assessment

The water stability of the as-synthesized photocatalyst was evaluated after photocatalysis. Following the completion of the photocatalytic experiments, the residue was washed three times with ethanol to separate the photocatalyst from the pollutants and then dried at 150 °C for 2 h. The obtained product was subsequently analyzed employing XRD, UV-vis absorbance, and XPS techniques.

2.4 Computational framework

The electronic band structure, density of states, and optical properties of CSB and CSB′B nanocrystals were investigated using DFT calculations employing both the standard generalized gradient approximation (GGA) and GGA+U methods based on the PBE gradient corrected exchange–correlation functional.[36] The calculations were performed by implementing the experimentally obtained structural parameters. Accordingly, the pristine $CsSnBr_3$ unit cell was optimized in its cubic phase. In order to observe the impact of Bi^{3+} doping, a 2 × 2 × 2 supercell of CSB replaced one Sn atom with one Bi atom, which resulted in 12.5% doping. In this investigation, the DFT-based plane wave pseudo-potential (PWPP) as implemented in the Cambridge Serial Total Energy Package (CASTEP) was used.[37] A kinetic cut-off of 500 and 312.9 eV was used for describing the unit cell and doped supercell, respectively. Additionally, Monkhorst–Pack grids of 12 × 12 × 12 and 6 × 6 × 6 *k* mesh were implemented for the optimization of the formulated unit and supercell. The convergence thresholds for the geometry optimization were (a) a total energy of 5.0×10^{-6} eV per atom, (b) a maximum force of 0.01 eV $Å^{-1}$, (c) a maximum stress of 0.02 GPa, and (d) a maximum displacement of 5.0×10^{-6} Å.

3 Results and discussion

3.1 Experimental investigation

3.1.1 Crystal structure analysis. The Rietveld refined[38] XRD spectra of the synthesized samples are illustrated in Fig. 2 and the structural parameters of the as-synthesized nanocrystals as obtained *via* the refinement have been tabulated in Table 1.

For the CSB sample, all the diffraction peaks are indexed to a cubic perovskite phase (space group $Pm\bar{3}m$) with $a = b = c =$

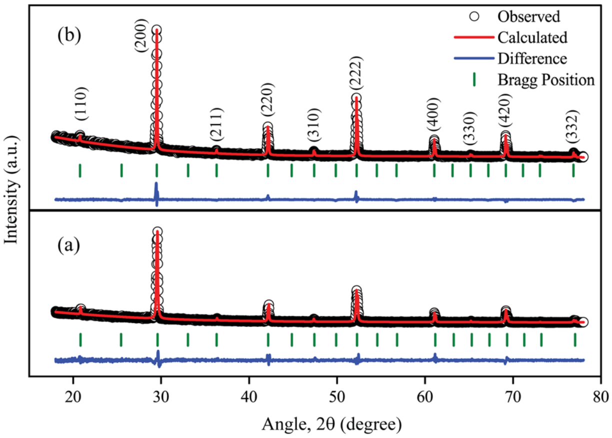

Fig. 2 Comparison between the observed and calculated XRD patterns of (a) CSB and (b) CSB′B samples.

6.052 Å and $\alpha = \beta = \gamma = 90°$. The prominent peaks at 29.46°, 42.16°, 52.27°, and 69.31° are attributed to the (200), (220), (222), and (420) crystal planes (JCPDS file no. 70-1645) of the CSB sample, respectively.[39] Additionally, no undesired peaks were found in the XRD pattern indicating the successful synthesis of phase-pure CSB followed by the hot injection method. Moreover, the similar XRD patterns of the CSB and CSB′B samples (Fig. 2(b)) suggested that the doping did not alter the periodic arrangement of the lattice.[40] However, a higher doping concentration of 10% led to the emergence of an impurity peak in the XRD pattern (ESI (Fig. S1†)), which was also reported in an analogous investigation.[18] Since the synthesis environment in the hot injection technique was maintained strictly, the impurity peak in the XRD pattern of the 10% doped Bi sample can merely be attributed to the formation of a newly formed compound, which might lead to erroneous results.[16,41] Hence, we conducted further characterization of the CSB and 5 mol% Bi-doped CSB samples only.

Notably, based on previous investigations,[42,43] we expected a lattice shrinkage due to the incorporation of Bi^{3+} having a smaller effective ionic radius of 0.103 nm than Sn^{2+} (0.110 nm).[44] However, in this investigation, we have observed that compared to CSB, the peaks of CSB′B shifted toward lower 2θ values (ESI Fig. S2†), suggesting a lattice expansion. This unusual phenomenon can be ascribed to the stereochemical activity of the dopant, bismuth.[45] For a better understanding of how stereochemically active bismuth caused volume expansion, the partial density of states of bismuth-doped samples was calculated using DFT, which will be discussed in the Theoretical investigation section. The calculation revealed that the Bi^{3+} 6s and 6p orbitals became hybridized with Br^- 2p orbitals, which led to the formation of a strong covalent bond and the resulting structural strain of the original $[SnBr_6]^{4-}$ framework is released by elongating the lattice parameters. For comparing the structural strain in the synthesized samples, the extent of microstrain was quantified by analyzing the three major peaks of the diffraction patterns of both CSB and CSB′B samples implementing the Williamson–Hall method[46] and is depicted in the ESI (Fig. S3†). From the calculation, it was evident that the bismuth doping almost doubled the structural strain and the consistent increase indicates that the strain was uniform in nature throughout the lattice, which led to the expansion of the unit cell volume of the CSB′B sample. Furthermore, the change in structural stability was theoretically predicated using the Goldschmidt tolerance factor (τ)[47] stated as:

$$\tau = \frac{R_{A-X}}{\sqrt{2}R_{B-X}} \tag{1}$$

where R_{A-X} and R_{B-X} are the bond lengths between A and X, and B and X ions, respectively. The bond lengths were obtained from the Theoretical investigation part and the calculated τ value for the CSB sample was 0.940, which agrees with a previously reported result[48] and the tolerance factor slightly increases to 0.943 owing to the incorporation of bismuth. This result indicates that the CSB′B sample should exhibit better structural stability than the CSB sample.

3.1.2 Chemical state analyses.

In order to investigate the doping effect of Bi^{3+} on the CSB perovskite, we have characterized the CSB′B sample using XPS. The XPS full survey spectrum of CSB′B nanocrystals has been illustrated in Fig. 3(a) which verified the presence of all the desired elements. The Bi 4f peak (Fig. 3(b)) revealed the presence of the dopant bismuth in the CSB′B sample and the peaks at ∼159.1 and ∼164.9 eV indicated that the dopant has a +3 oxidation state.[49] For Cs 3d, two distinct peaks can be observed at the binding energies of ∼726.4 and ∼740.3 eV (Fig. 3(c)). The Cs $3d_{5/2}$ and Cs $3d_{3/2}$ states indicated that Cs was present in a +1 state.[50] Moreover, Fig. 3(d) reveals the core level spectra of the Sn 3d orbital. The observed peaks at ∼486.4 and ∼494.8 eV were fitted with Gaussian fitting where the difference between the peaks indicated the presence of the Sn^{2+} state only.[51] Thus, it can be anticipated that Bi doping has inhibited the oxidation of Sn^{2+}, which is regarded as the most common problem in $CsSnBr_3$ related to optoelectronic applications. It is noteworthy that the Sn $3d_{5/2}$ and $3d_{3/2}$ peaks slightly shifted toward lower binding energy than the reported value of Sn in $CsSnBr_3$.[21] These shifts signify the change in chemical bonding properties due to the incorporation of Bi^{3+}.[52] Therefore, from both XRD and XPS results, it can be verified that the dopant Bi^{3+} has been effectively substituted in the $CsSnBr_3$ lattice rather than only physical mixing.[53,54]

Table 1 Structural parameters of CSB and CSB′B nanocrystals as obtained *via* Rietveld refinement of the XRD pattern

Sample	Lattice parameters (Å)	Unit cell volume (Å^3)	Space group	Goodness of fit (χ^2)
CSB	6.052	221.757	$Pm\bar{3}m$	2.54
CSB′B	6.066	223.236	$Pm\bar{3}m$	1.88

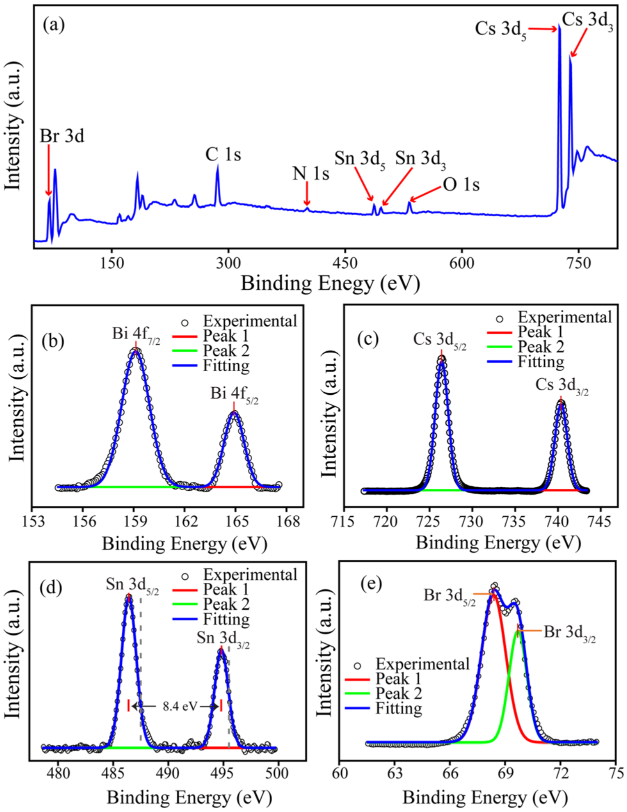

Fig. 3 (a) Full survey spectrum of XPS analysis; narrow spectra of (b) Bi 4f, (c) Cs 3d, (d) Sn 3d (dashed grey lines are the peak values from ref. 21), and (e) Br 3d for the CSB′B nanocrystals.

Furthermore, the Br 3d core level peak was deconvoluted into two symmetric Gaussian peaks at ∼68.4 and ∼69.7 eV (Fig. 3(e)). The peak of lower binding energy is associated with the Br $3d_{5/2}$ state and the higher one is with the Br $3d_{3/2}$ state.[55]

3.1.3 Thermal stability analysis. To study the effect of bismuth doping on the thermal properties of the CSB perovskite, thermogravimetric analysis on both pristine and doped samples was carried out and is presented in Fig. 4. Both CSB and CSB′B showed a very similar as well as nominal weight loss tendency over a wide range of temperature, from 30 to 200 °C. This weight loss can be attributed to the evaporation of residual water and organic species, in particular organic ligands used in the synthesis and purification processes.[56,57] From Fig. 4, it can be observed that the inflection temperature of CSB′B is around 200 °C, which is lower than that of CSB (∼290 °C). Interestingly, above the inflection temperature, the CSB′B sample showed linear weight loss, whereas a sharp decrease was observed for the CSB sample. This rapid declination indicates the sublimation of the CSB sample.[58] On the other hand, the linear weight loss of CSB′B above the inflection temperature represents its superior thermal stability, which is in good agreement with the theoretically predicted structural stability factor as we demonstrated in the Crystal structure analysis section. This superior stability of the CSB′B sample might be due to its reduced cuboctahedral void due to the substitution of Sn by smaller Bi ions.[47] From eqn (1), it is obvious that the atomic radius of Sn and Br governs the size of $[\mathrm{SnBr_6}]^{4-}$ octahedra, hence determining the size of the cuboctahedral void for Cs cations. When the large Sn atoms were replaced by smaller Bi atoms, the cuboctahedral void reduced resulting in a more stable cubic crystal structure than the CSB sample, which was evident from the smaller weight loss in TGA analysis (Fig. 4).

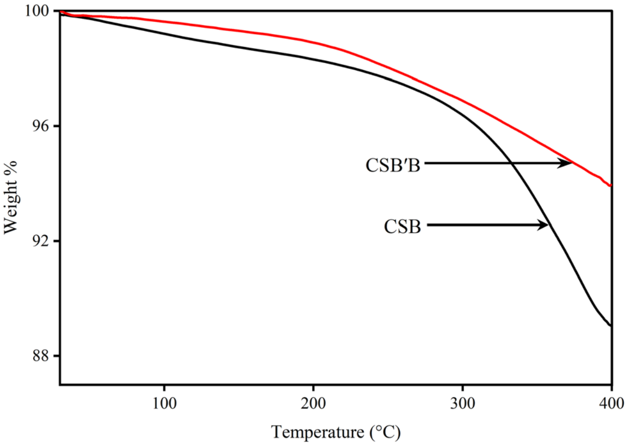

Fig. 4 TGA curves of CSB and CSB′B samples.

3.1.4 Morphological and elemental analyses. From the morphological analysis conducted initially by FESEM imaging, it can be observed that the CSB sample Fig. 5(a) consists of agglomerated as well as larger crystals of ∼316 nm. However, a radical change has been observed due to the incorporation of bismuth, and the synthesized nanocrystals became less agglomerated and the average particle size reduced to ∼87 nm (ESI Fig. S4†). Although the reaction cut-off time for synthesizing the sample was strictly maintained to be equal, this reduction in particle size indicates that the doping might have inhibited the crystal growth. When the dopants were introduced into the precursor solution, they acted as foreign elements, and the crystal formation had to occur along with the dopants.[59] In the case of CSB′B, the ionic radius of the substituent Bi is smaller than that of Sn (0.110 nm for $\mathrm{Sn^{2+}}$ and 0.103 nm for $\mathrm{Bi^{3+}}$) and Bi is more electronegative than Sn (2.02 for Bi and 1.96 for Sn). The more electronegative element Bi is less reactive than Sn, which in turn reduced the growth rate of CSB′B,[60] leading to the formation of small-sized particles with an average size of ∼87 nm.

EDX analyses demonstrated the presence of all the required elements in the as-synthesized samples. The mass and atomic percentages of each element in CSB and CSB′B as obtained from EDX were consistent with the theoretical values and are provided in ESI Tables S1 and S2.† Moreover, the presence of all the desired elements (Cs, Bi, Sn, and Br) was also observed in the XPS full survey spectra (Fig. 3(a)) demonstrating that the elemental compositions of CSB′B fitted well with that observed from EDX analysis. Fig. 6 shows the high-resolution TEM images and SAED patterns of the as-synthesized CSB and CSB′B samples. The calculated inter-planar spacing was found to be 0.302 and 0.303 nm, for CSB and CSB′B, respectively, which matched well with the (200) crystal plane of the respective

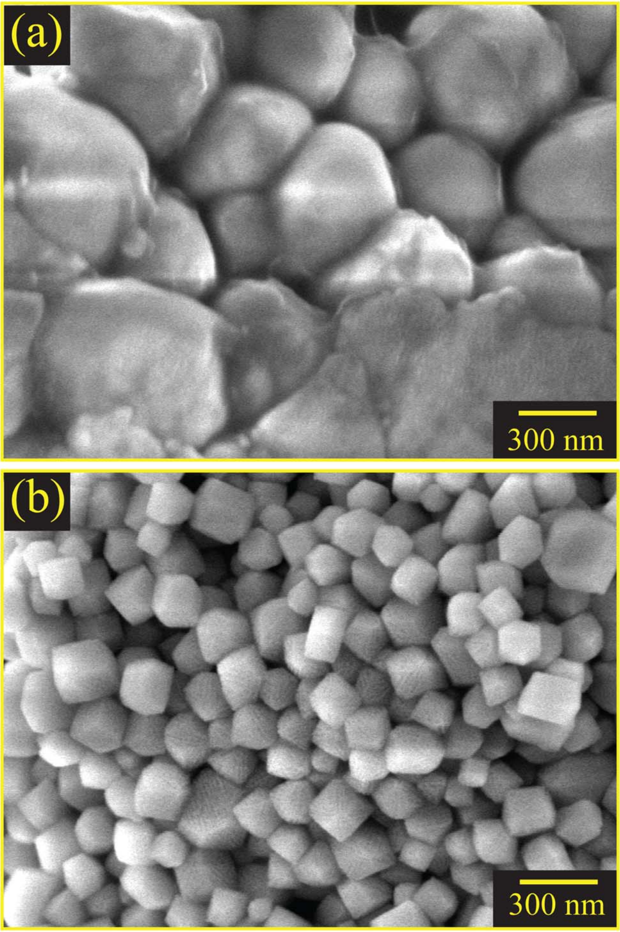

Fig. 5 FESEM images of (a) CSB and (b) CSB′B samples, respectively.

samples. The slight increase in the inter-planar spacing measured for the (200) plane of CSB′B further validated the trend of increasing lattice parameters observed in the XRD analysis. Moreover, the bright diffraction rings in the representative SAED patterns (Fig. 6(c) and (d)) revealed the polycrystalline nature of both samples. The diffraction rings of both samples could be assigned to the (200), (211), (220), and (420) crystal planes, which are in agreement with the XRD results. The interplanar spacings or *d*-spacings obtained by analyzing the SAED patterns of the prepared samples were further compared with those obtained from the XRD pattern of the pristine sample and are tabulated in the ESI (Table S3†).

3.1.5 Optical properties. From the optical absorbance curve of the as-synthesized samples, as depicted in Fig. 7(a), it can be stated that the CSB′B sample was able to absorb a higher percentage of UV photons compared to the CSB one. This superior UV absorption ability suggests that the CSB′B material can utilize solar energy more efficiently than the CSB sample. Notably, a sharp peak near ∼380 nm indicates that a trace amount of bismuth has the ability to modify the electronic transition of CSB perovskite. This peak can be attributed to the characteristics $5s^2$ to $5s^15p^1$ absorption transitions of $[BiBr_6]^{3-}$ octahedra. An electronic transition in the ions with lone pair ns^2 has been reported to occur *via* five different energy levels, including the ground state ($^1S_0$) and the excitation state (sp), which further splits into four energy levels, namely, $^1P_1$, $^3P_0$, $^3P_1$, and $^3P_2$.[61] In between those energy levels, the transition between $^1S_0$ and $^1P_1$ is allowed, and the $^1S_0$ to $^3P_1$ transition is partially allowed due to spin–orbit coupling for heavy atoms, while the $^1S_0$ to $^3P_2$ and $^1S_0$ to $^3P_0$ transitions are totally forbidden. Therefore, the absorption peak at ∼380 nm can be attributed to the partially allowed transition from $^1S_0$ to $^3P_1$ of Bi^{3+}.

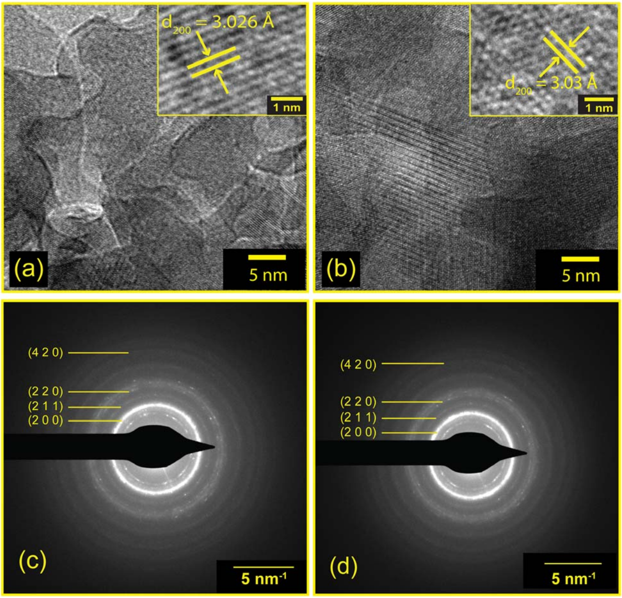

Fig. 6 Bright field HRTEM images and SAED patterns of (a) and (c) CSB and (b) and (d) CSB′B samples.

Next, the absorbance data were employed to determine the direct band gap of the prepared samples using the Tauc relationship.[23,62] From the Tauc plots (Fig. 7(b)), the optical band gaps were estimated to be ∼1.89 and ∼1.73 eV for CSB and CSB′B, respectively, suggesting bismuth doping at the Sn

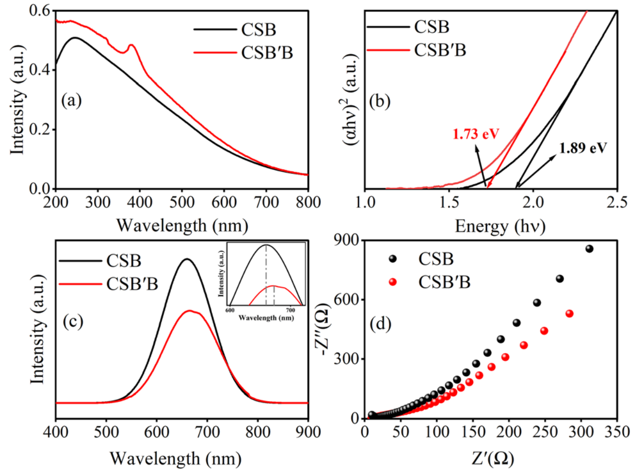

Fig. 7 Optical absorption spectrum of (a) CSB and CSB′B, (b) Tauc plot, (c) steady-state PL spectra for the prepared samples (inset shows a PL peak shift due to doping), and (d) Nyquist plots of CSB and CSB′B.

site of $CsSnBr_3$ perovskite has narrowed down the band gap of the respective sample. In the theoretical calculation part of this investigation, the detailed mechanism of this band gap reduction has been explained.

After comprehending the effect of Bi doping on the CSB band gap, we investigated how this modification affected the materials' photoluminescence properties. Fig. 7(c) illustrates the PL emission spectra of CSB and CSB′B samples suspended in ethanol, where the pristine CSB showed higher emission intensity than the Bi-doped CSB′B sample. Doping is anticipated to increase the energy levels reducing the band gap and simultaneously decreasing the recombination rate of electrons–holes due to which intensity decreases and peaks become broader as can be seen in Fig. 7(c).

Additionally, we have observed a difference between the band gap calculated from UV-vis absorbance (1.73 eV) and PL peak energy (1.84 eV) for the CSB′B sample (Fig. 7(b) and (c)). This difference in the absorbance edge and PL peak might be attributed to 'Stokes Shift' which was also reported by analogous investigations on halide perovskite materials.[63–65] Moreover, previous studies[66,67] reported that PL intensity is inversely proportional to the charge carrier separation efficiency of the sample, and hence, the suppressed PL intensity of the CSB′B sample indicates its better charge separation ability. This enhanced charge separation ability is expected to directly influence the photocatalytic properties of the doped sample.[66] In order to further support the enhanced charge separation of the CSB′B sample, EIS was carried out and the results are depicted in Fig. 7(d). The smaller Nernst radius of the CSB′B sample in Fig. 7(d) indicates a lower charge transfer resistance compared to that of CSB, demonstrating the highest charge transfer efficiency.[68–70]

3.1.6 Analyzing band-edge positions. To assess the potentiality of CSB and CSB′B samples in a practical application *i.e.*, the photocatalytic dye degradation, at first, the band edge positions were estimated by adopting the Mulliken electronegativity approach.[71] The conduction band minimum (CBM) and valence band maximum (VBM) potential *vs.* the normal hydrogen electrode (NHE) of the CSB sample were calculated to be −0.18 and +1.71 eV, respectively. The Bi doping caused the shifting of the CB toward a lower position and the VB to a higher position, and thus for the CSB′B sample, the values of the CBM and VBM were found to be −0.1 and +1.63 eV, respectively. An energy band diagram provided in Fig. 8(a) based on the results from the Mulliken electronegativity approach depicts the values of the CBM and VBM along with the redox potentials of different redox half reactions of interest.

To experimentally obtain band edge positions, Mott–Schottky analysis was carried out at a frequency of 200 Hz and the results are depicted in Fig. 8(b). The quasi-linear behavior as observed in Fig. 8(b) indicates the characteristics of n-type semiconductors.[72] Considering the negligible difference between the flat band (V_{fb}) and the conduction band for n-type semiconductors, the determined V_{fb} can be approximated as the CB edge ($E_{cb} \approx V_{fb}$).[68] Hence, the CB potentials of CSB and CSB′B are located at −0.35 and −0.22 V *vs.* Ag/AgCl, which are further converted into −0.15 and −0.02 *vs.* NHE according to the equation $E_{NHE} = E_{Ag/AgCl} + 0.197$.[73] Compared to the CSB sample, the CB potentials of the CSB′B sample show a downward shift, which can be attributed to the effect of Bi doping. Additionally, the smaller slope of the CSB′B sample indicates a higher carrier concentration due to the substitution of Sn^{2+} with Bi^{3+}, which acts as an electron donor. The valence band level of CSB and CSB′B is calculated by using $E_g + E_{cb}$ to be 1.74 and 1.71 eV, respectively. Although a difference was observed in the theoretical and experimental band edge positions, the trend of lowering the conduction band was observed in both cases.

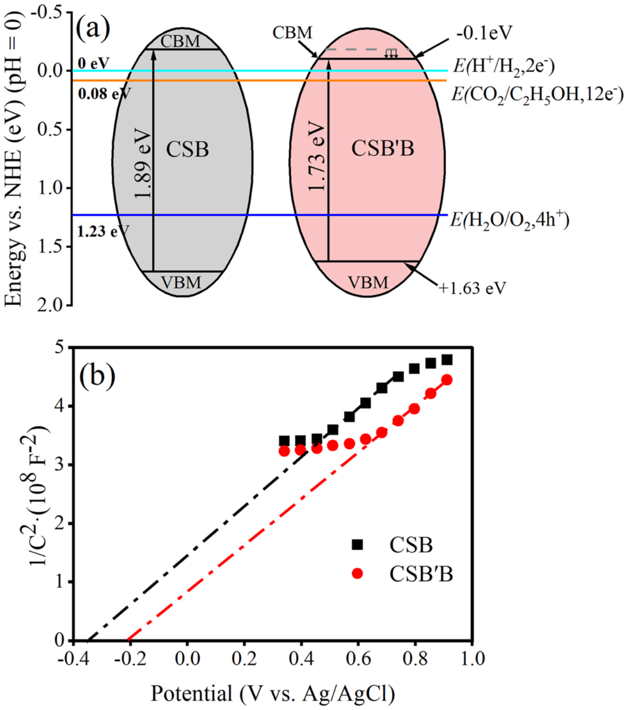

Fig. 8 Band-edge positions adopted from (a) Mulliken electronegativity calculation and (b) Mott–Schottky plots for CSB and CSB′B samples.

It is known that, for an ideal overall water-splitting reaction to occur, the VB and CB edge positions of a semiconductor must straddle the water oxidation and reduction potentials (CBM < 0 and VBM > 1.23 eV).[74] Clearly, both the CBM and VBM potentials as obtained from Mulliken electronegativity and Mott–Schottky approaches of the prepared samples satisfy the required criteria, which indicates their promising potential for photocatalytic water splitting.[75,76] Another possible application of the as-synthesized nanocrystals could be converting CO_2 into fuels like ethanol and methane.[77]

3.1.7 Photocatalytic performance evaluation. To demonstrate the solar light driven application of the synthesized nanocrystals, their photodegradation ability toward the degradation of a commonly used dye, RhB, was evaluated as a test case. For thorough investigation, the dye degradation performance of CSB and CSB′B was tested under both UV-vis and visible spectra and the performances were compared with that of a commercially available photocatalyst, P25 titania. Before including any photocatalyst in the dye solution, the selfdecomposition rate of RhB was determined under identical conditions and only 4% RhB degradation was recorded after 240 min, which is in good agreement with a previous study.[66]

From the absorbance curve depicted in Fig. 9(a) and (b), it can be observed that the peak intensity of the spectra was reduced with respect to time following a hypsochromic shift, which indicates the deterioration of RhB solution under the UV-vis spectrum due to the inclusion of CSB and CSB′B samples, respectively. Previous investigation[24] on the photodegradation performance of halide perovskite has reported that RhB commonly degrades in two competitive and co-existing pathways: (1) destruction of the conjugated structure of RhB and (2) *N*-deethylation, the formation of *N*-deethylated intermediates in a stepwise manner during the degradation process. Accordingly, the reduction in the peak intensity and the hypsochromic shift observed in Fig. 9(a) and (b) indicates that the RhB degraded in both pathways. Additionally, a similar trend of declining peak intensity was also noticed in the UV region of the absorbance curve (ESI Fig. S5†), further confirming the destruction of the xanthene rings of RhB.[78] Moreover, from Fig. 9(c), a proportional relationship has been observed between the degradation efficiency and peak shift of absorption spectra suggesting that the *N*-deethylation process plays a vital role after a certain period. However, when the CSB′B sample was used, the smallest peak shift indicated that the *N*-deethylation process was the least among all the other photocatalysts. In order to determine the degradation efficiency of the samples, C/C_0 *vs.* irradiation time was plotted (Fig. 9(d)), where C_0 is the initial concentration of RhB solution and C is the concentration at a specific time, t (30–240 min). Evidently, for the CSB′B sample, the degradation efficiency was better compared to the CSB sample, which could be ascribed to the smaller particle size and reduced band gap as well as the increased e^- and h^+ recombination rate of CSB′B due to Bi doping. Noticeably, under UV-vis illumination, P25 nanoparticles showed a significantly higher RhB degradation rate compared to the synthesized nanocrystals, which could be due to their smaller particle size of 25 nm as well as the wide band gap of ~3.0 eV.[79] However, this

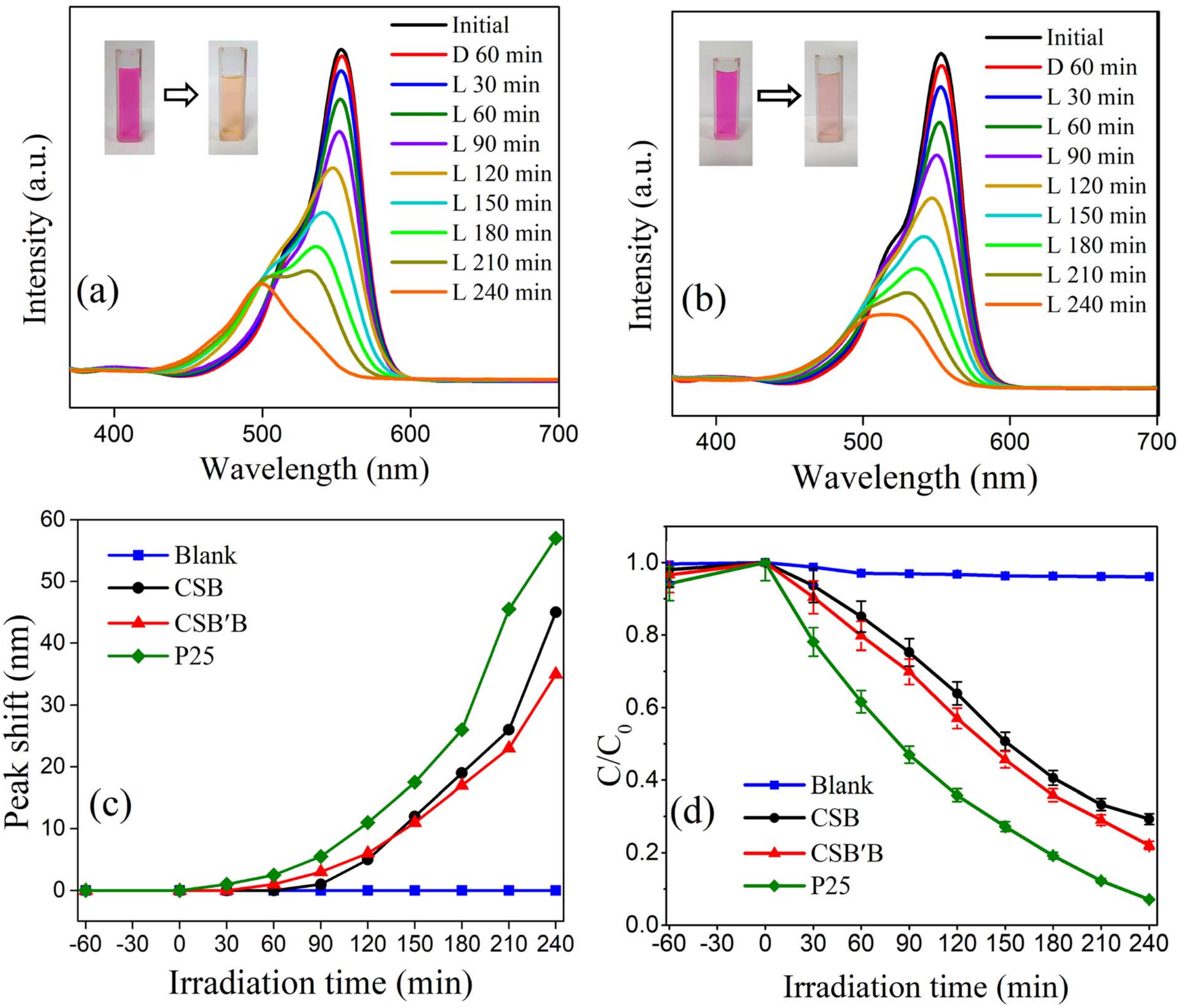

Fig. 9 Spectral changes during the deterioration of RhB solution utilizing (a) CSB and (b) CSB′B nanocrystals under UV-vis irradiation, (c) peak shift observed in the absorbance spectrum of RhB solution for different photocatalysts, and (d) the degradation efficiency of different photocatalysts as a function of irradiation time.

large band gap of P25 nanoparticles has limited their application only to the UV region ($\lambda < 400$ nm), which comprises ~4% of the solar energy.[80]

Therefore, the performance of the synthesized samples and P25 was evaluated under visible irradiation which comprises 42.3% of the solar spectra, and the results are displayed in Fig. 10. Noticeably, the peak shift of RhB absorbance spectra was also observed under visible irradiation (Fig. 10(a)), but in this case, the shift was less prominent suggesting the destruction of the conjugated structure to be the main pathway under visible light. Interestingly, under visible irradiation, a drastic reduction in the degradation efficiency (Fig. 10(b)) was observed for P25, which is obvious because of its wide band gap. Notably, the CSB′B sample retained almost 50% of its initial degradation rate under visible irradiation, and the performance of the Bi-doped sample still surpassed that of the pristine one. The profound photocatalytic activity of the Bi-doped CSB photocatalyst under visible irradiation suggests its potential utilization in visible light-mediated applications. Additionally, the experimental data were fitted to a pseudo-first-order kinetics model for quantitative investigation of the kinetics of RhB dye degradation under solar irradiation.[81] The calculated rate constants (k) for the degradation of RhB using P25 and the as-synthesized photocatalysts were calculated and values are inserted in ESI Table S4.†

To monitor the dye sensitization phenomena under simulated solar irradiation, the decomposition rate of a colorless pollutant, CIP, using the CSB′B sample was also investigated. As can be seen in ESI Fig. S6,† almost 72% degradation of CIP was monitored under UV-vis irradiation. These results clearly showed the degradation performances of the as-synthesized photocatalysts were governed by photocatalysis rather than dye sensitization, as the colorless CIP is unable to sensitize a photocatalytic reaction under solar illumination.[82]

3.1.8 Stability of the photocatalyst. Noticeably, metal halide perovskites are unstable upon moisture and water exposure, and the stability issue ultimately limits their photocatalytic and related applications in an aqueous environment. In recent years, evidence of water stability in lead-free metal halide perovskites was reported. Particularly, some Bi-based and Sn-based perovskites have shown promising photocatalytic properties, and they were stable in water.[83–85] Therefore, in this investigation, the water stability of the nanocrystals was checked utilizing the recovered CSB′B powders after the

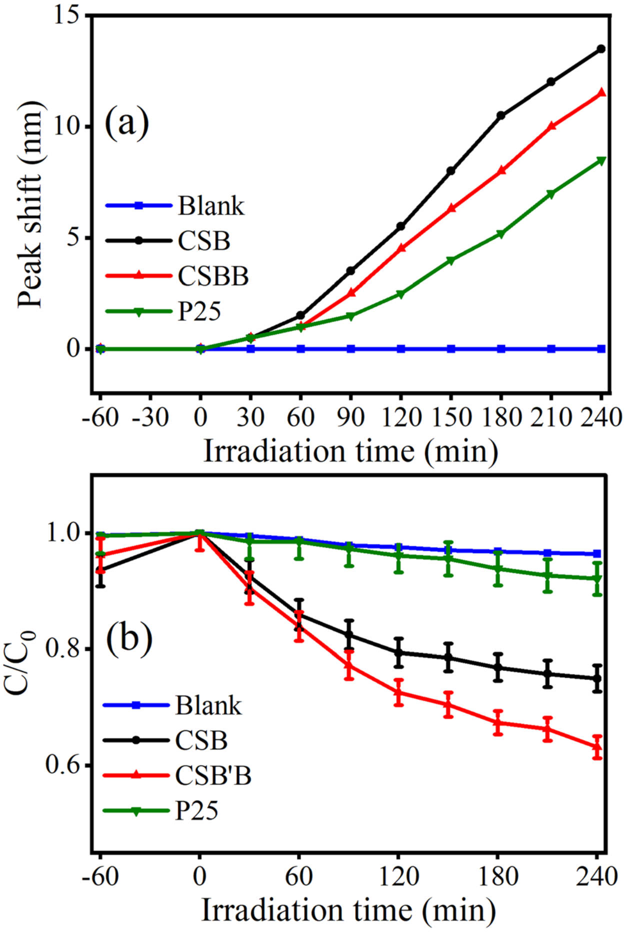

Fig. 10 (a) Peak shift observed in the absorbance spectrum of RhB solution for different photocatalysts and (b) degradation efficiency of RhB as a function of irradiation time for different photocatalysts under visible irradiation.

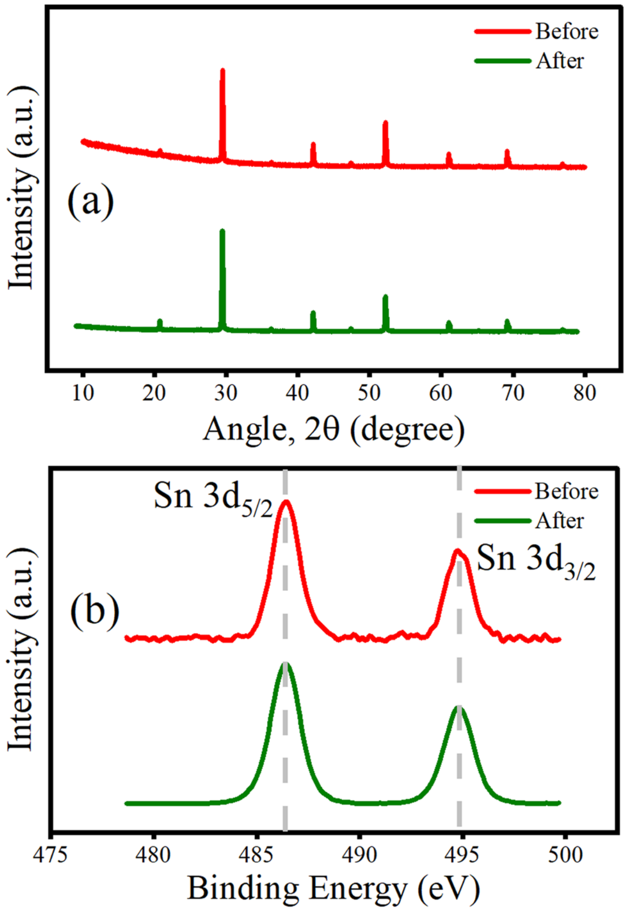

Fig. 11 (a) XRD patterns and (b) narrow scan XPS spectra of the Sn 3d orbital before and after photocatalytic degradation of RhB in an aqueous medium by the CSB′B sample.

photocatalytic degradation of RhB dye that underwent XRD analysis (Fig. 11(a)). Comparing the XRD patterns of CSB′B before and after photocatalysis, we may claim that the material kept its original crystal structure even after 4 hours of solar irradiation in aqueous medium. In addition, we have captured the UV-vis absorbance spectrum of the CSB′B sample before and after catalytic treatments in water. Interestingly, the optical band gap of the CSB′B sample after photocatalysis was ~1.72 eV, which is very close to the optical band gap (1.73 eV) prior to the use of the material in photocatalysis.

According to previous reports,[13,86] the oxidation of Sn^{2+} to Sn^{4+} also limits the performance and stability of Sn-based MHPs. Additionally, a recent investigation clearly demonstrates that metal doping suppresses the oxidation of Sn^{2+} to Sn^{4+} in lead-free perovskites, which in turn may stabilize tin-based halide perovskites.[87] Therefore, for a further confirmation of the water stability of Bi-doped CSB′B perovskite and suppression of the oxidative degradation of Sn, XPS analysis of the synthesized material was performed after photocatalysis. Fig. 11(b) shows the Sn 3d spectra of the as-prepared sample (red line) and the sample after photocatalysis (green line). The overlapping spectra, with an unchanged shape and position of the peak (Sn $3d_{5/2}$ at ~486 eV), clearly demonstrate that the as-synthesized CSB′B is stable under aqueous medium and also confirms the +2 oxidation state of Sn without any evidence of oxidation of the sample. Based on a previous investigation,[88] we assume that upon coming into direct contact with water, some of the CSB′B breaks into constituent Cs^+ cations and $SnBr_x$ and $BiBr_x$ complex anions.[88] These complexes might form strong bonds with the water molecules, creating an amorphous surface layer.[89] This amorphous surface layer protected the rest of the core CSB′B nanocrystals from degrading. As a result, the sample was able to retain its structural, optical properties, and oxidation state as well and it was able to produce enough electron–hole pairs for the photocatalytic pollutant degradation process. Our experimental findings provide the evidence of the water stability of the CSB′B material after photocatalysis.

3.1.9 Photocatalytic dye degradation mechanism. To elucidate the underlying mechanism for the dye degradation reactions, we have performed active species trapping experiments under UV-vis irradiation and the results are depicted in ESI Fig. S7.† From the figure, it can be observed that when IPA was used to quench the $^{\bullet}OH$, there was no significant change in the degradation rate, which was expected due to the smaller VBM potential of the synthesized materials. Additionally, as observed from supplementary Fig. S7,† when the electrons and $^{\bullet}O_2^-$ were quenched, the degradation drops to about 60%, which was about 80% without using any scavengers. It can be anticipated that, when the photo-generated electrons were trapped, they could not react with the O_2 adsorbed on the surface to form superoxide radicals ($^{\bullet}O_2^-$). Furthermore, when superoxide radicals were confined using acrylamide, they were unable not take part in the degradation reactions to break the dye molecules. As a result, the photocatalytic dye degradation efficiency drops noticeably. Interestingly, the presence of EDTA–2Na (hole scavenger) suppressed the degradation performance drastically, which revealed that the holes were the major species for the dye degradation. According to previous investigations,[90,91] holes can directly oxidize the dye molecules using the following series of chain reactions:

$$\text{Photoexcitation: CSB}'\text{B} + h\nu \rightarrow e^- + h^+ \tag{2}$$

$$\text{Photoexcited } e^- \text{ scavenging: } (O_2)_{ads} + e^- \rightarrow {}^{\bullet}O_2^- \tag{3}$$

$$\text{Degradation by } O_2^-\text{: pollutants} + {}^{\bullet}O_2^- \rightarrow \text{degradation product} \tag{4}$$

$$\text{Degradation by photoholes: pollutants} + h^+ \rightarrow [\text{pollutant}]^+ \tag{5}$$

$$[\text{Pollutant}]^+ \rightarrow \text{degradation product} \tag{6}$$

This pathway is thermodynamically feasible when the oxidative potential of the dye is lower than the semiconductors' VB edge.[92,93] Since, the oxidative potential of RhB (1.36 eV *vs.* NHE, pH = 0)[78] is lower than the valence band of both samples (1.74 and 1.71 eV for CSB and CSB′B, respectively), both of the samples are able to directly oxidize the organic pollutant RhB and subsequently degrade the dye into less harmful by-products. In all the photocatalytic degradation experiments, the CSB′B sample performed better than the CSB sample under both UV-vis and visible irradiation. This superior performance can be attributed to a couple of factors such as the smaller band gap, which allows the absorption of a wider range of the solar spectrum, smaller particle size, and the newly formed shallow state in the CB due to Bi doping (Fig. 14), which might have acted as an electron trapping site and captured the excited electrons to enable the e^-–h^+ separation. As a result, the photogenerated electrons migrated from the Bi dopant to the surface of the photocatalyst could react with the absorbed oxygen and then reduce it to superoxide radicals.

$$\text{Bi} + e^- \rightarrow e^-(\text{trapped}) \tag{7}$$

$$e^-(\text{trapped}) + O_2 \rightarrow {}^{\bullet}O_2^- \tag{8}$$

These radicals will react with the pollutant promoting the total degradation rate. Fig. 12 shows a schematic dye degradation mechanism of the CSB′B photocatalyst.

3.2 Theoretical investigation

The introduction of Bi^{3+} into the CSB lattice has resulted in several noticeable modifications in the structural, morphological, optical, and photocatalytic properties of the pristine sample as stated in the aforementioned Experimental sections. These findings further inspired us to investigate the effect of doping at the atomic level. Notably, it is very difficult to experimentally observe the doping effect at such an elementary level. Therefore, in this investigation, DFT-based first-principles calculations were performed to analyze the effect of doping on the electronic band structures and optical properties of CSB and CSB′B samples using experimentally obtained parameters.

3.2.1 Density of states of CSB and CSB′B perovskites. The unit cell volume expansion as well as the reduction in particle

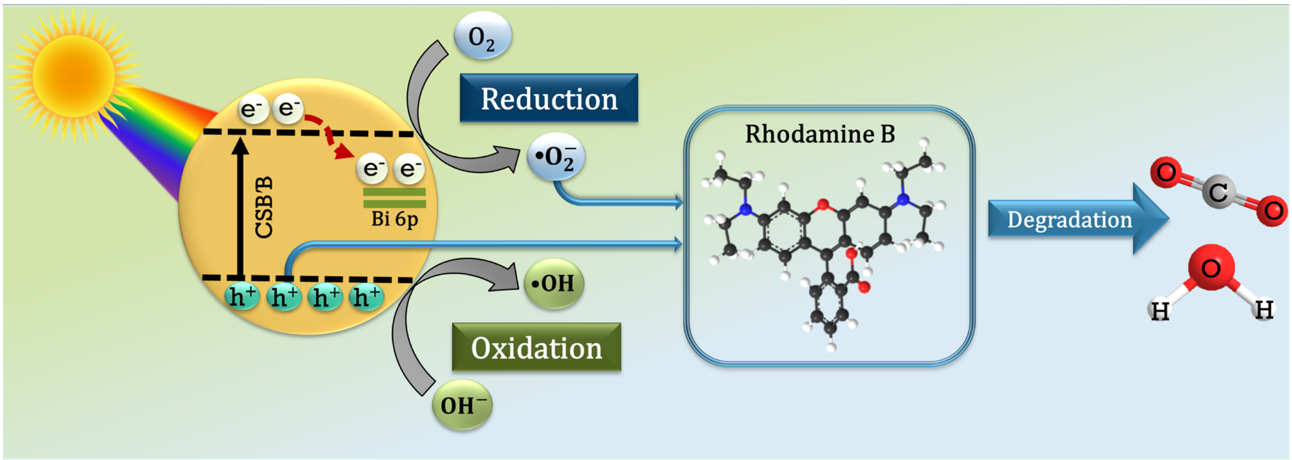

Fig. 12 Schematic representation of the proposed dye degradation mechanism by the CSB′B sample.

size due to doping can be well explained by performing partial density of states (PDOS) calculations using the GGA method on both CSB and CSB′B samples. From Fig. 13(a), it can be observed that the VB (E_F < 0 eV) of the CSB sample is made up of the hybridization of Br 4p and Sn 5p orbitals, with the majority of the contribution coming from Br 4p states. On the other hand, the CB (E_F > 0 eV) was dominated by the Sn 5p orbital, with a minor contribution from Cs 6s.

Notably, from the calculated PDOS of the CSB′B sample (Fig. 13(b)), it can be observed that the dopant bismuth had an influence on both the CB and VB. To be precise, the VB of the CSB′B sample has an additional contribution from the Bi 6p orbitals, and still, the major contribution was from Sn 5p. Although the 5p orbital has lower energy than the 6p orbital, when the redox potential and electronegativity of Bi are taken into account, the empty Bi-6p orbital has lower energy than the empty Sn-5p orbital.[17,94] As a result, the bottom edge of the CB shifts downward due to bismuth doping. Additionally, a shallow state made up of the hybridization between Bi 6p and Br 4p (as observed in the magnified image of Fig. 13(b)) has appeared in the CB, which indicates the formation of a new bond (details of this bond nature are discussed in ESI S5†) between the dopant and surrounding halogen anions. The formation of the new bond might be responsible for lowering the experimentally obtained optical band gap of the CSB′B sample.

3.2.2 Electronic band structures and optical properties. From the calculated band structures for CSB and CSB′B samples (Fig. 14), it was found that the bismuth doping has reduced the electronic band gap from 0.686 to 0.469 eV. This reduction in the band gap might be attributed to the appearance of new energy bands in the conduction level. In addition to that, the newly emerged electronic bands in the CB might have acted as electron trapping sites, which in turn enhanced the photocatalytic performance of the CSB′B sample by trapping the photogenerated electrons and reducing the recombination of electron–hole pairs.[67,95,96] This result of suppressed recombination is also in good agreement with the findings from PL spectroscopy. Furthermore, the theoretical calculations revealed that the optical band gap of CSB and CSB′B samples is 1.23 and 1.02 eV, respectively. Comparing the experimental and

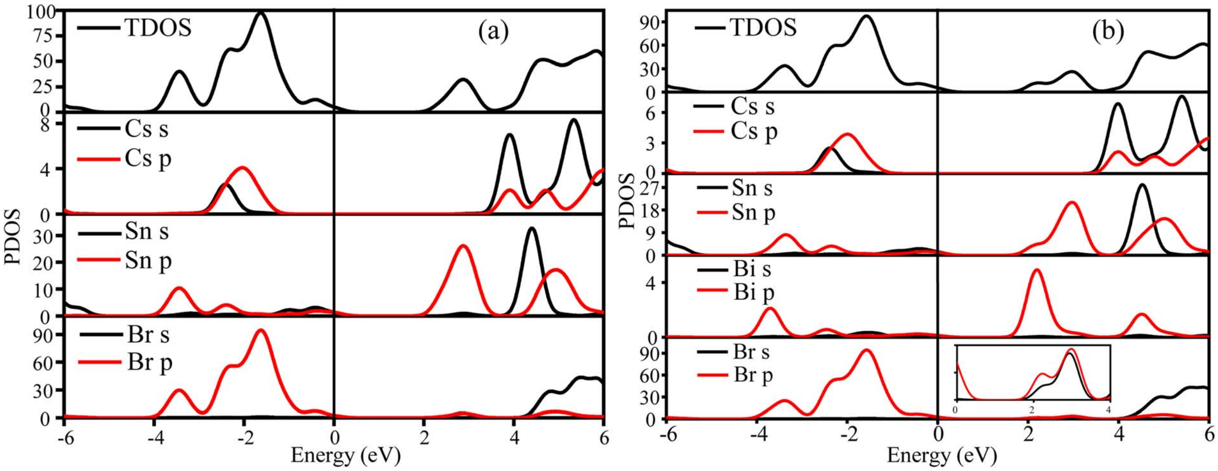

Fig. 13 The calculated TDOS PDOS of the (a) CSB and (b) CSB′B samples, respectively. The magnified image in the figure (b) depicts the Br s and p orbitals of CSB′B.

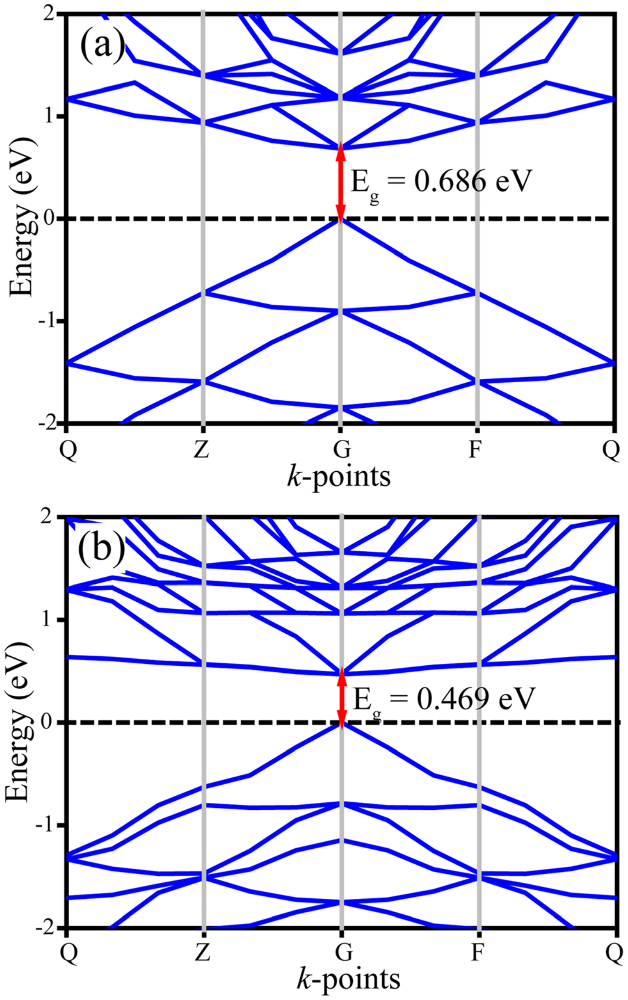

Fig. 14 The calculated electronic band structure of (a) CSB and (b) CSB′B samples.

theoretical values of the optical band gaps, a deviation of ∼35% was observed. Such underestimation of the optical band gap was also observed in similar GGA-based calculations on analogous materials.[24,97] The obtained values of the structural, electronic, and optical properties of CSB and CSB′B samples calculated using the GGA functional are tabulated in ESI Table S5.†

Notably, regardless of the underestimation, the reduction nature of the optical band gap due to doping is in good qualitative agreement with the experimentally obtained values. The underestimation tendency of the GGA method in calculating the optical band gap has inspired us to conduct additional computations considering the effect of on-site Coulomb interaction and exchange–correlation functions (U_{eff}) on the CSB sample in order to improve the accuracy of the theoretical calculations. The obtained values of the structural, electronic, and optical properties of the CSB sample for different U_{eff} values are tabulated and illustrated in the ESI (Table S6, Fig. S9, and S10†). It is worth noting that, as the value of U_{eff} increases, the theoretical predictions get closer to the experimentally obtained values, and at $U_{\mathrm{eff}} = 4$ eV, the calculated structural parameters, optical and electronic band gaps agree well with the experimentally obtained values.

However, using the GGA+U method to account for on-site Coulomb interaction and exchange–correlation functions significantly increased the computational cost, limiting this study to investigating the effect of U_{eff} on the CSB sample only. Nevertheless, based on the results achieved for the CSB sample, we have anticipated that the calculation incorporating U_{eff} on the Bi-doped sample might provide values that will be in good qualitative agreement with the experiments.

4 Conclusions

We have successfully synthesized lead-free $CsSnBr_3$ and 5 mol% Bi-doped $CsSnBr_3$ nanocrystals using a facile hot injection technique. The incorporation of Bi in $CsSnBr_3$ inhibited the transformation of valence states from Sn^{2+} to Sn^{4+}, a significant reduction in the size of the nanocrystals, and a decrease in the optical band gap as well as PL intensity. The thermal stability was also found to be increased due to Bi doping. Interestingly, the visible-light-driven degradation efficiency of CSB′B is almost five times higher than that of a widely investigated photocatalyst, P25 nanoparticles. Additionally, the degradation of the colorless probe ciprofloxacin by the CSB′B photocatalyst confirmed that the degradation is photocatalytic and not dye-sensitized. The enhanced photocatalytic performance of the CSB′B nanocrystals might be attributed to their smaller particle size, suitable band gap, and prolonged charge carrier recombination. Also the unaltered XRD and Sn 3d XPS patterns of the CSB′B sample after photocatalysis verified their promising water stability. Furthermore, DFT-based analysis revealed the emergence of new bands in the conduction band due to doping that might have acted as electron trapping sites and played a significant role in improving the catalytic efficiency of the doped samples. The outcome of this investigation may propose new perspectives for improving the stability, morphology, and visible-light-driven applications of CSB and analogous perovskites *via* doping at the B site.

Author contributions

Md. Asif Adib: methodology, investigation, writing – original draft, and formal analysis. Fahmida Sharmin: writing – review editing and formal analysis. M. A. Basith: conceptualization, resources, writing – review editing, and supervision.

Conflicts of interest

There are no conflicts to declare.

Acknowledgements

We sincerely acknowledge the Bangladesh University of Engineering and Technology (BUET) for providing financial assistance through CASR and also as a Basic Research Grant. We are thankful to the Institute of Information and Technology, BUET for its computational facilities.

References

1 G. Li, G. Wang, Y. Zhang, J. Shen and B. Zhang, Tunable resonance of a graphene-perovskite terahertz metasurface, *Nanoscale Adv.*, 2023, **5**, 756–766.

2 S. Sansoni, F. M. Anoè and M. Meneghetti, Simple and sustainable synthesis of perovskite-based optoelectronic material: $CsPbBr_3$ nanocrystals via laser ablation in alcohol, *Nanoscale Adv.*, 2022, **4**, 5009–5014.

3 A. Babayigit, A. Ethirajan, M. Muller and B. Conings, Toxicity of organometal halide perovskite solar cells, *Nat. Mater.*, 2016, **15**, 247–251.

4 Z. Jin, Z. Zhang, J. Xiu, H. Song, T. Gatti and Z. He, A critical review on bismuth and antimony halide based perovskites and their derivatives for photovoltaic applications: recent advances and challenges, *J. Mater. Chem. A*, 2020, **8**, 16166–16188.

5 M. Li, X. Zhang, K. Matras-Postolek, H. S. Chen and P. Yang, An anion-driven Sn^{2+} exchange reaction in $CsPbBr_3$ nanocrystals towards tunable and high photoluminescence, *J. Mater. Chem. C*, 2018, **6**, 5506–5513.

6 K. Thirumal, H. Ding, C. Yan, L. Wei, T. Baikie, L. Zhang, M. Sherburne, S. Li, M. Asta and N. Mathews, Lead-free germanium iodide perovskite materials for photovoltaic application, *J. Mater. Chem. A*, 2015, **3**, 23829–23832.

7 M.-G. Ju, M. Chen, Y. Zhou, H. F. Garces, J. Dai, L. Ma, N. P. Padture and X. C. Zeng, Earth-abundant nontoxic titanium (IV)-based vacancy-ordered double perovskite halides with tunable 1.0 to 1.8 eV bandgaps for photovoltaic applications, *ACS Energy Lett.*, 2018, **3**, 297–304.

8 Z. Zhu, C.-C. Chueh, N. Li, C. Mao and A. K.-Y. Jen, Realizing efficient lead-free formamidinium tin triiodide perovskite solar cells via a sequential deposition route, *Adv. Mater.*, 2018, **30**, 1703800.

9 H. Yao, F. Zhou, Z. Li, Z. Ci, L. Ding and Z. Jin, Strategies for improving the stability of tin-based perovskite ($ASnX_3$) solar cells, *Adv. Sci.*, 2020, **7**, 1903540.

10 J. Barrett, S. Bird, J. Donaldson and J. Silver, The Mössbauer effect in tin (II) compounds. Part XI. The spectra of cubic trihalogenostannates (II), *J. Chem. Soc. A*, 1971, 3105–3108.

11 C. C. Stoumpos, C. D. Malliakas and M. G. Kanatzidis, Semiconducting tin and lead iodide perovskites with organic cations: phase transitions, high mobilities, and near-infrared photoluminescent properties, *Inorg. Chem.*, 2013, **52**, 9019–9038.

12 G. Nasti and A. Abate, Tin halide perovskite ($ASnX_3$) solar cells: a comprehensive guide toward the highest power conversion efficiency, *Adv. Energy Mater.*, 2020, **10**, 1902467.

13 J. Pascual, G. Nasti, M. H. Aldamasy, J. A. Smith, M. Flatken, N. Phung, D. Di Girolamo, S.-H. Turren-Cruz, M. Li, A. Dallmann, et al., Origin of Sn (II) oxidation in tin halide perovskites, *Mater. Adv.*, 2020, **1**, 1066–1070.

14 M. Chen, M. G. Ju, H. F. Garces, A. D. Carl, L. K. Ono, Z. Hawash, Y. Zhang, T. Shen, Y. Qi, R. L. Grimm, D. Pacifici, X. C. Zeng, Y. Zhou and N. P. Padture, Highly stable and efficient all-inorganic lead-free perovskite solar cells with native-oxide passivation, *Nat. Commun.*, 2019, **10**, 1–8.

15 A. Bala and V. Kumar, A Study of Eu Doping in Nanolayers of $CsPbBr_3$ using Ab Initio Calculations to Understand f–f Transitions in Eu^{3+}-Doped Nanocrystals for Light-Emitting Diodes, *ACS Appl. Nano Mater.*, 2020, **3**, 4437–4444.

16 M. Lee, B. Yoo, J. Im, T. Hyeon and I. Chung, Electronic Band Engineering via MI_3 (M = Sb, Bi) Doping Remarkably Enhances the Air Stability of Perovskite $CsSnI_3$, *ACS Appl. Energy Mater.*, 2020, **3**, 10477–10484.

17 H. Hasegawa, K. Kobayashi, Y. Takahashi, J. Harada and T. Inabe, Effective band gap tuning by foreign metal doping in hybrid tin iodide perovskites, *J. Mater. Chem. C*, 2017, **5**, 4048–4052.

18 Y. Hu, F. Bai, X. Liu, Q. Ji, X. Miao, T. Qiu and S. Zhang, Bismuth Incorporation Stabilized α-$CsPbI_3$ for Fully Inorganic Perovskite Solar Cells, *ACS Energy Lett.*, 2017, **2**, 2219–2227.

19 J. Shamsi, A. S. Urban, M. Imran, L. De Trizio and L. Manna, Metal Halide Perovskite Nanocrystals: Synthesis, Post-Synthesis Modifications, and Their Optical Properties, *Chem. Rev.*, 2019, **119**, 3296–3348.

20 M. Saski, D. Prochowicz, W. Marynowski and J. Lewiński, Mechanosynthesis, Optical, and Morphological Properties of MA, FA, $CsSnX_3$ (X = I, Br) and Phase-Pure Mixed-Halide $MASnI_xBr_{3-x}$ Perovskites, *Eur. J. Inorg. Chem.*, 2019, **2019**, 2680–2684.

21 S. Gupta, T. Bendikov, G. Hodes and D. Cahen, CsSnBr3, A Lead-Free Halide Perovskite for Long-Term Solar Cell Application: Insights on SnF_2 Addition, *ACS Energy Lett.*, 2016, **1**, 1028–1033.

22 L. Protesescu, S. Yakunin, M. I. Bodnarchuk, F. Krieg, R. Caputo, C. H. Hendon, R. X. Yang, A. Walsh and M. V. Kovalenko, Nanocrystals of Cesium Lead Halide Perovskites ($CsPbX_3$, X = Cl, Br, and I): Novel Optoelectronic Materials Showing Bright Emission with Wide Color Gamut, *Nano Lett.*, 2015, **15**, 3692–3696.

23 T. C. Jellicoe, J. M. Richter, H. F. Glass, M. Tabachnyk, R. Brady, S. E. Dutton, A. Rao, R. H. Friend, D. Credgington, N. C. Greenham, et al., Synthesis and Optical Properties of Lead-Free Cesium Tin Halide Perovskite Nanocrystals, *J. Am. Chem. Soc.*, 2016, **138**, 2941–2944.

24 M. S. Ali, S. Das, Y. F. Abed and M. A. Basith, Lead-free $CsSnCl_3$ perovskite nanocrystals: rapid synthesis, experimental characterization and DFT simulations, *Phys. Chem. Chem. Phys.*, 2021, **23**, 22184–22198.

25 K. Mahesh, C.-Y. Chang, W.-L. Hong, T.-H. Wen, P.-H. Lo, H.-Z. Chiu, C.-L. Hsu, S.-F. Horng and Y.-C. Chao, Lead-free cesium tin halide nanocrystals for light-emitting diodes and color down conversion, *RSC Adv.*, 2020, **10**, 37161–37167.

26 N. Phung, R. Félix, D. Meggiolaro, A. Al-Ashouri, G. Sousa e Silva, C. Hartmann, J. Hidalgo, H. Kobler, E. Mosconi, B. Lai, et al., The Doping Mechanism of Halide Perovskite Unveiled by Alkaline Earth Metals, *J. Am. Chem. Soc.*, 2020, **142**, 2364–2374.

27 M. Nazim, A. A. P. Khan, F. Khan, S. K. Cho and R. Ahmad, Insertion of metal cations into hybrid organometallic halide perovskite nanocrystals for enhanced stability: eco-friendly synthesis, lattice strain engineering, and defect chemistry studies, *Nanoscale Adv.*, 2022, **4**, 2729–2743.

28 J. Yuan, H. Liu, S. Wang and X. Li, How to apply metal halide perovskites to photocatalysis: challenges and development, *Nanoscale*, 2021, **13**, 10281–10304.

29 M. Shaban, M. Rabia, M. G. Eldakrory, R. M. Maree and A. M. Ahmed, Efficient photoselectrochemical hydrogen production utilizing of $APbI_3$ (A= Na, Cs, and Li) perovskites nanorods, *Int. J. Energy Res.*, 2021, **45**, 7436–7446.

30 D. Cardenas-Morcoso, A. F. Gualdron-Reyes, A. B. Ferreira Vitoreti, M. García-Tecedor, S. J. Yoon, M. Solis de la Fuente, I. Mora-Sero and S. Gimenez, Photocatalytic and photoelectrochemical degradation of organic compounds with all-inorganic metal halide perovskite quantum dots, *J. Phys. Chem. Lett.*, 2019, **10**, 630–636.

31 K. Ren, S. Yue, C. Li, Z. Fang, K. A. Gasem, J. Leszczynski, S. Qu, Z. Wang and M. Fan, Metal halide perovskites for photocatalysis applications, *J. Mater. Chem. A*, 2022, **10**, 407–429.

32 A. Swarnkar, A. R. Marshall, E. M. Sanehira, B. D. Chernomordik, D. T. Moore, J. A. Christians, T. Chakrabarti and J. M. Luther, Quantum dot–induced phase stabilization of α-$CsPbI_3$ perovskite for high-efficiency photovoltaics, *Science*, 2016, **354**, 92–95.

33 Y. Zhang, T. D. Siegler, C. J. Thomas, M. K. Abney, T. Shah, A. De Gorostiza, R. M. Greene and B. A. Korgel, A "tips and tricks" practical guide to the synthesis of metal halide perovskite nanocrystals, *Chem. Mater.*, 2020, **32**, 5410–5423.

34 J. Rodríguez-Carvajal, Recent advances in magnetic structure determination by neutron powder diffraction, *Phys. B*, 1993, **192**, 55–69.

35 M. Klinger, More features, more tools, more CrysTBox, *J. Appl. Crystallogr.*, 2017, **50**, 1226–1234.

36 J. P. Perdew, J. A. Chevary, S. H. Vosko, K. A. Jackson, M. R. Pederson, D. J. Singh and C. Fiolhais, Atoms, molecules, solids, and surfaces: applications of the generalized gradient approximation for exchange and correlation, *Phys. Rev. B: Condens. Matter Mater. Phys.*, 1992, **46**, 6671.

37 S. J. Clark, M. D. Segall, C. J. Pickard, P. J. Hasnip, M. I. Probert, K. Refson and M. C. Payne, First principles methods using CASTEP, *Z. Kristallogr. - Cryst. Mater.*, 2005, **220**, 567–570.

38 H. M. Rietveld, A profile refinement method for nuclear and magnetic structures, *J. Appl. Crystallogr.*, 1969, **2**, 65–71.

39 L. Peedikakkandy and P. Bhargava, Composition dependent optical, structural and photoluminescence characteristics of cesium tin halide perovskites, *RSC Adv.*, 2016, **6**, 19857–19860.

40 R. Ahsan, A. Mitra, S. Omar, M. Z. R. Khan and M. A. Basith, Sol-gel synthesis of $DyCrO_3$ and 10% Fe-doped $DyCrO_3$ nanoparticles with enhanced photocatalytic hydrogen production abilities, *RSC Adv.*, 2018, **8**, 14258–14267.

41 K. Vighnesh, S. Wang, H. Liu and A. L. Rogach, Hot-Injection Synthesis Protocol for Green-Emitting Cesium Lead Bromide Perovskite Nanocrystals, *ACS Nano*, 2022, **12**, 19618–19625.

42 Q. Wei, J. Yin, O. M. Bakr, Z. Wang, C. Wang, O. F. Mohammed, M. Li and G. Xing, Effect of Zinc-doping on the Reduction of the Hot-carrier Cooling Rate in Halide Perovskites, *Angew. Chem., Int. Ed.*, 2021, **60**, 10957–10963.

43 X. Miao, T. Qiu, S. Zhang, H. Ma, Y. Hu, F. Bai and Z. Wu, Air-stable $CsPb_{1-x}Bi_xBr_3$ ($0 \leq x \ll 1$) perovskite crystals: optoelectronic and photostriction properties, *J. Mater. Chem. C*, 2017, **5**, 4931–4939.

44 R. D. Shannon, Revised effective ionic radii and systematic studies of interatomic distances in halides and chalcogenides, *Acta Crystallogr., Sect. A: Cryst. Phys., Diffr., Theor. Gen. Crystallogr.*, 1976, **32**, 751–767.

45 P. Jiang, J. C. Neuefeind, M. Avdeev, Q. Huang, M. Yue, X. Yang, R. Cong and T. Yang, Unprecedented lattice volume expansion on doping stereochemically active Pb^{2+} into uniaxially strained structure of $CaBa_{1-x}Pb_xZn_2Ga_2O_7$, *Nat. Commun.*, 2020, **11**, 1–7.

46 Y. Zhao and J. Zhang, Microstrain and grain-size analysis from diffraction peak width and graphical derivation of high-pressure thermomechanics, *J. Appl. Crystallogr.*, 2008, **41**, 1095–1108.

47 A. Swarnkar, W. J. Mir and A. Nag, Can B-Site Doping or Alloying Improve Thermal- and Phase-Stability of All-Inorganic $CsPbX_3$ (X = Cl, Br, I) Perovskites?, *ACS Energy Lett.*, 2018, **3**, 286–289.

48 W. Travis, E. Glover, H. Bronstein, D. Scanlon and R. Palgrave, On the application of the tolerance factor to inorganic and hybrid halide perovskites: a revised system, *Chem. Sci.*, 2016, **7**, 4548–4556.

49 W. E. Morgan, W. J. Stec and J. R. Van Wazer, Inner-orbital binding-energy shifts of antimony and bismuth compounds, *Inorg. Chem.*, 1973, **12**, 953–955.

50 Q. Zhang, M. Tai, Y. Zhou, Y. Zhou, Y. Wei, C. Tan, Z. Wu, J. Li and H. Lin, Enhanced Photocatalytic Property of γ-$CsPbI_3$ Perovskite Nanocrystals with WS_2, *ACS Sustain. Chem. Eng.*, 2019, **8**, 1219–1229.

51 Z. Hong, D. Tan, R. A. John, Y. K. E. Tay, Y. K. T. Ho, X. Zhao, T. C. Sum, N. Mathews, F. García and H. S. Soo, Completely solvent-free protocols to access phase-pure, metastable metal halide perovskites and functional photodetectors from the precursor salts, *iScience*, 2019, **16**, 312–325.

52 S. S. Mali, J. V. Patil, J. A. Steele, S. R. Rondiya, N. Y. Dzade and C. K. Hong, Implementing dopant-free hole-transporting layers and metal-incorporated $CsPbI_2Br$ for stable all-inorganic perovskite solar cells, *ACS Energy Lett.*, 2021, **6**, 778–788.

53 M. I. Ustinova, M. M. Mikheeva, G. V. Shilov, N. N. Dremova, L. Frolova, K. J. Stevenson, S. M. Aldoshin and P. A. Troshin, Partial substitution of Pb^{3+} in $CsPbI_3$ as an efficient strategy to design fairly stable all-inorganic perovskite formulations, *ACS Appl. Mater. Interfaces*, 2021, **13**, 5184–5194.

54 J. V. Patil, S. S. Mali, D. W. Park and C. K. Hong, Novel ytterbium-doped $CsPbI_2Br$ thin-films–based inorganic

perovskite solar cells toward improved phase stability, *Mater. Today Chem.*, 2021, **22**, 100557.

55 M. Li, X. Zhang, K. Matras-Postolek, H.-S. Chen and P. Yang, An anion-driven Sn^{2+} exchange reaction in $CsPbBr_3$ nanocrystals towards tunable and high photoluminescence, *J. Mater. Chem. C*, 2018, **6**, 5506–5513.

56 S. Dastidar, C. J. Hawley, A. D. Dillon, A. D. Gutierrez-Perez, J. E. Spanier and A. T. Fafarman, Quantitative Phase-Change Thermodynamics and Metastability of Perovskite-Phase Cesium Lead Iodide, *J. Phys. Chem. Lett.*, 2017, **8**, 1278–1282.

57 J. B. Hoffman, G. Zaiats, I. Wappes and P. V. Kamat, $CsPbBr_3$ Solar Cells: Controlled Film Growth through Layer-by-Layer Quantum Dot Deposition, *Chem. Mater.*, 2017, **29**, 9767–9774.

58 F. Liu, C. Ding, Y. Zhang, T. S. Ripolles, T. Kamisaka, T. Toyoda, S. Hayase, T. Minemoto, K. Yoshino, S. Dai, et al., Colloidal Synthesis of Air-Stable Alloyed $CsSn_{1-x}Pb_xI_3$ Perovskite Nanocrystals for Use in Solar Cells, *J. Am. Chem. Soc.*, 2017, **139**, 16708–16719.

59 M. Sakar, S. Balakumar, P. Saravanan and S. Bharathkumar, Compliments of confinements: substitution and dimension induced magnetic origin and band-bending mediated photocatalytic enhancements in $Bi_{1-x}Dy_xFeO_3$ particulate and fiber nanostructures, *Nanoscale*, 2015, **7**, 10667–10679.

60 R. Sagheer, M. Khalil, V. Abbas, Z. N. Kayani, U. Tariq and F. Ashraf, Effect of Mg doping on structural, morphological, optical and thermal properties of ZnO nanoparticles, *Optik*, 2020, **200**, 163428.

61 A. Noculak, V. Morad, K. M. McCall, S. Yakunin, Y. Shynkarenko, M. Worle and M. V. Kovalenko, Bright blue and green luminescence of Sb (III) in double perovskite Cs_2MInCl_6 (M= Na, K) matrices, *Chem. Mater.*, 2020, **32**, 5118–5124.

62 J. Tauc, R. Grigorovici and A. Vancu, Optical Properties and Electronic Structure of Amorphous Germanium, *Phys. Status Solidi B*, 1966, **15**, 627–637.

63 T. Cai, J. Wang, W. Li, K. Hills-Kimball, H. Yang, Y. Nagaoka, Y. Yuan, R. Zia and O. Chen, Mn^{2+}/Yb^{3+} codoped $CsPbCl_3$ perovskite nanocrystals with triple-wavelength emission for luminescent solar concentrators, *Adv. Sci.*, 2020, **7**, 2001317.

64 B. Zhou, Z. Liu, S. Fang, J. Nie, H. Zhong, H. Hu, H. Li and Y. Shi, Emission mechanism of self-trapped excitons in Sb^{3+}-doped all-inorganic metal-halide perovskites, *J. Phys. Chem. Lett.*, 2022, **13**, 9140–9147.

65 S. Gull, M. H. Jamil, X. Zhang, H.-s. Kwok and G. Li, Stokes shift in inorganic lead halide perovskites: current status and perspective, *ChemistryOpen*, 2022, **11**, e202100285.

66 F. Sharmin and M. A. Basith, Simple low temperature technique to synthesize sillenite bismuth ferrite with promising photocatalytic performance, *ACS Omega*, 2022, **7**, 34901–34911.

67 C. Guo, K. Tian, L. Wang, F. Liang, F. Wang, D. Chen, J. Ning, Y. Zhong and Y. Hu, Approach of fermi level and electron-trap level in cadmium sulfide nanorods via molybdenum doping with enhanced carrier separation for boosted photocatalytic hydrogen production, *J. Colloid Interface Sci.*, 2021, **583**, 661–671.

68 R. Liu, J. Ren, D. Zhao, J. Ning, Z. Zhang, Y. Wang, Y. Zhong, C. Zheng and Y. Hu, Band-gap engineering of porous $BiVO_4$ nanoshuttles by Fe and Mo co-doping for efficient photocatalytic water oxidation, *Inorg. Chem. Front.*, 2017, **4**, 2045–2054.

69 M. Ni, Y. Zhu, C. Guo, D.-L. Chen, J. Ning, Y. Zhong and Y. Hu, Efficient Visible-Light-Driven CO_2 Methanation with Self-Regenerated Oxygen Vacancies in $Co_3O_4/NiCo_2O_4$ Hetero-Nanocages: Vacancy-Mediated Selective Photocatalysis, *ACS Catal.*, 2023, **13**, 2502–2512.

70 S. Ullah, Q. Li, R. Ullah, S. Anwar, M. F. Hameed and M. Zhu, Facile synthesis of water-soluble silver nanoclusters for the photocatalytic degradation of dyes by multivariate optimization approach, *Nanoscale Adv.*, 2023, **5**, 3326–3335.

71 M. D. I. Bhuyan, S. Das and M. A. Basith, Sol-gel synthesized double perovskite Gd_2FeCrO_6 nanoparticles: structural, magnetic and optical properties, *J. Alloys Compd.*, 2021, **878**, 160389.

72 E. Gao, W. Wang, M. Shang and J. Xu, Synthesis and enhanced photocatalytic performance of graphene-Bi_2WO_6 composite, *Phys. Chem. Chem. Phys.*, 2011, **13**, 2887–2893.

73 C. Wan, L. Zhou, L. Sun, L. Xu, D.-g. Cheng, F. Chen, X. Zhan and Y. Yang, Boosting visible-light-driven hydrogen evolution from formic acid over AgPd/2D g-C_3N_4 nanosheets Mott-Schottky photocatalyst, *J. Chem. Eng.*, 2020, **396**, 125229.

74 A. Ganguly, O. Anjaneyulu, K. Ojha and A. K. Ganguli, Oxide-based nanostructures for photocatalytic and electrocatalytic applications, *CrystEngComm*, 2015, **17**, 8978–9001.

75 A. G. Tamirat, J. Rick, A. A. Dubale, W.-N. Su and B.-J. Hwang, Using hematite for photoelectrochemical water splitting: a review of current progress and challenges, *Nanoscale Horiz.*, 2016, **1**, 243–267.

76 S. Acharya, S. Martha, P. C. Sahoo and K. Parida, Glimpses of the modification of perovskite with graphene-analogous materials in photocatalytic applications, *Inorg. Chem. Front.*, 2015, **2**, 807–823.

77 E. Kalamaras, M. M. Maroto-Valer, M. Shao, J. Xuan and H. Wang, Solar carbon fuel via photoelectrochemistry, *Catal. Today*, 2018, **317**, 56–75.

78 M. Yin, Z. Li, J. Kou and Z. Zou, Mechanism investigation of visible light-induced degradation in a heterogeneous TiO_2/Eosin Y/Rhodamine B system, *Environ. Sci. Technol.*, 2009, **43**, 8361–8366.

79 H. Li, Y. Song, J. Zhang and J. He, Turbulence enhanced ferroelectric-nanocrystal-based photocatalysis in urchin-like $TiO_2/BaTiO_3$ microspheres for hydrogen evolution, *Nanoscale Adv.*, 2021, **3**, 5618–5625.

80 Q. Wang, Q. Gao, A. M. Al-Enizi, A. Nafady and S. Ma, Recent advances in MOF-based photocatalysis: environmental remediation under visible light, *Inorg. Chem. Front.*, 2020, **7**, 300–339.

81 D. F. Ollis, Kinetics of liquid phase photocatalyzed reactions: an illuminating approach, *J. Phys. Chem. B*, 2005, **109**, 2439–2444.

82 F. Sharmin, F. Ara and M. A. Basith, Comparison of the structure-property relationships between sillenite and

perovskite phases of $Bi_{0.9}Dy_{0.1}FeO_3$ nanostructures, *New J. Chem.*, 2023, **47**, 4707–4719.

83 L. Romani, A. Speltini, F. Ambrosio, E. Mosconi, A. Profumo, M. Marelli, S. Margadonna, A. Milella, F. Fracassi, A. Listorti, F. De Angelis and L. Malavasi, Water-Stable $DMASnBr_3$ Lead-Free Perovskite for Effective Solar-Driven Photocatalysis, *Angew. Chem., Int. Ed. Engl.*, 2021, 3611–3618.

84 H. Zhao, Y. Li, B. Zhang, T. Xu and C. Wang, $PtI_x/[(CH_3)_2NH_3]_3[BiI_6]$ as a well-dispersed photocatalyst for hydrogen production in hydroiodic acid, *Nano Energy*, 2018, **50**, 665–674.

85 D. Ricciarelli, W. Kaiser, E. Mosconi, J. Wiktor, M. W. Ashraf, L. Malavasi, F. Ambrosio and F. De Angelis, Reaction mechanism of photocatalytic hydrogen production at water/tin halide perovskite interfaces, *ACS Energy Lett.*, 2022, **7**, 1308–1315.

86 N. K. Noel, S. D. Stranks, A. Abate, C. Wehrenfennig, S. Guarnera, A.-A. Haghighirad, A. Sadhanala, G. E. Eperon, S. K. Pathak, M. B. Johnston, et al., Lead-free organic–inorganic tin halide perovskites for photovoltaic applications, *Energy Environ. Sci.*, 2014, **7**, 3061–3068.

87 C. Park, J. Choi, J. Min and K. Cho, Suppression of oxidative degradation of tin–lead hybrid organometal halide perovskite solar cells by Ag doping, *ACS Energy Lett.*, 2020, **5**, 3285–3294.

88 H. Huang, B. Pradhan, J. Hofkens, M. B. Roeffaers and J. A. Steele, Solar-driven metal halide perovskite photocatalysis: design, stability, and performance, *ACS Energy Lett.*, 2020, **5**, 1107–1123.

89 W. Kaiser, D. Ricciarelli, E. Mosconi, A. A. Alothman, F. Ambrosio and F. De Angelis, Stability of tin-versus lead-halide perovskites: Ab initio molecular dynamics simulations of perovskite/water interfaces, *J. Phys. Chem. Lett.*, 2022, **13**, 2321–2329.

90 M. Y. Guo, A. M. C. Ng, F. Liu, A. B. Djurišić and W. K. Chan, Photocatalytic activity of metal oxides—the role of holes and OH radicals, *Appl. Catal., B*, 2011, **107**, 150–157.

91 F. Opoku, K. K. Govender, C. G. C. E. van Sittert and P. P. Govender, Recent progress in the development of semiconductor-based photocatalyst materials for applications in photocatalytic water splitting and degradation of pollutants, *Adv. Sustainable Syst.*, 2017, **1**, 1700006.

92 K. Rajeshwar, M. Osugi, W. Chanmanee, C. Chenthamarakshan, M. V. B. Zanoni, P. Kajitvichyanukul and R. Krishnan-Ayer, Heterogeneous photocatalytic treatment of organic dyes in air and aqueous media, *J. Photochem. Photobiol., C*, 2008, **9**, 171–192.

93 Y. Chen, S. Yang, K. Wang and L. Lou, Role of primary active species and TiO_2 surface characteristic in UV-illuminated photodegradation of Acid Orange 7, *J. Photochem. Photobiol., A*, 2005, **172**, 47–54.

94 A. J. Bard, *Standard Potentials in Aqueous Solution (Monographs in Electroanalytical Chemistry and Electrochemistr)*, CRC Press, New York, USA, 1st edn, 1985.

95 M. Ni, H. Zhang, S. Khan, X. Chen, F. Chen, C. Guo, Y. Zhong and Y. Hu, In-situ photodeposition of cadmium sulfide nanocrystals on manganese dioxide nanorods with rich oxygen vacancies for boosting water-to-oxygen photooxidation, *J. Colloid Interface Sci.*, 2022, **613**, 764–774.

96 R. Shi, H.-F. Ye, F. Liang, Z. Wang, K. Li, Y. Weng, Z. Lin, W.-F. Fu, C.-M. Che and Y. Chen, Interstitial P-doped CdS with long-lived photogenerated electrons for photocatalytic water splitting without sacrificial agents, *Adv. Mater.*, 2018, **30**, 1705941.

97 R. Devi, B. Singh, P. Canepa and G. Sai Gautam, Effect of exchange-correlation functionals on the estimation of migration barriers in battery materials, *npj Comput. Mater.*, 2022, **8**, 1–13.